1995PASP..107..184L

Publications of the Astronomical Society of the Pacific
107: 184–192, 1995 February

A New Fabry-Perot Spectrometer for Observations of Diffuse Near-Infrared Line Emission

M. L. LUHMAN, D. T. JAFFE, L. D. KELLER, AND SOOJONG PAK

Department of Astronomy, University of Texas, Austin, Texas 78712
Electronic mail: luhman@astro.as.utexas.edu, dtj@astro.as.utexas.edu, keller@astro.as.utexas.edu, soojong@astro.as.utexas.edu

Received 1994 October 18; accepted 1994 November 29

ABSTRACT. We describe a new Fabry-Perot spectrometer that is optimized for the detection of extended, low-surface-brightness line emission from 1.4 to 2.4 μm. The instrument combines high throughput and high sensitivity, yet limits the background radiation falling on the detector. The instrument has a single 20″–200″ beam and a resolving power $\lambda/\Delta\lambda \sim 2500$. The system is background shot-noise limited in the *K* window and limited by a combination of read noise, dark-current shot noise, and fluctuations in the OH airglow lines in the *H* window. We present sample data of some of the lowest-surface-brightness H_2 line emission in the near infrared obtained to date.

1. INTRODUCTION

Near-infrared spectroscopy has benefitted greatly from improvements in single-channel and array detectors during the last 25 years. These improvements have drastically lowered the detection threshold of infrared instruments (e.g., Hoffman and Woolaway 1994). The surface-brightness sensitivity of many modern-day infrared spectrometers and imagers is no longer limited by the noise associated with the detector and read-out electronics. Yet, many environments are still relatively unexplored in the near infrared, as the intrinsically faint line emission within these regions from important species such as H, H_2, He, and Fe often lies beyond the sensitivity range of existing instruments. Such environments include diffuse clouds, the outlying portions of giant molecular clouds (well away from the star-forming cores), and the global interstellar medium of nearby galaxies. Observations of these regions are quite common, however, in the far-infrared, sub-mm, and mm, where many low-excitation atomic and molecular lines are found.

To detect and map very low-surface-brightness line emission in the near infrared, we have constructed a new Fabry-Perot (FP) spectrometer. We designed the instrument for high throughput of the source signal, moderate spectral resolution ($\lambda/\Delta\lambda > 2000$), and low shot and read noise. The spectrometer design also significantly reduces the influence of sky noise arising from fluctuations in the OH airglow lines and in the thermal sky background, which often limit surface brightness sensitivity in the near infrared (Ramsey et al. 1992; Maihara 1993). The instrument is specifically intended for observations of diffuse line emission from very extended (>1′) sources. We describe the instrument in Sec. 2, achievement of optimal surface brightness sensitivity in Sec. 3, and observational procedures in Sec. 4. We present sample data in Sec. 5 and summarize the characteristics of our Fabry-Perot spectrometer in Sec. 6.

2. DESCRIPTION OF THE INSTRUMENT

Figure 1 shows a schematic representation of the instrument. The beam enters through the Cassegrain port of the telescope. A sliding mirror allows the spectrometer to look either at the telescope or at the calibration/alignment lamp. The beam then passes through an IR-grade fused silica (SiO_2) collimating lens (Infrared Optical Products). Several collimators with focal lengths of 343, 457, and 838 mm are available to couple the instrument foreoptics to various telescopes, including the McDonald Observatory 0.9-m and 2.7-m and several IR-optimized telescopes such as the KPNO 1.3 m, CTIO 1.5 m, Steward Observatory 1.55 m, and IRTF 3 m. A gold-coated flat mirror redirects the beam into either an *H*- or *K*-band Fabry-Perot interferometer (Burleigh Instruments Inc., Model TL-38). Both *H*- and *K*-band FPs rest on a common translation stage for easy interchange during observations. The *H*- and *K*-band FPs operate in ~120th and ~90th order, respectively, and have a finesse of 25–30. In the Appendix, we discuss the real-time control and alignment of the FP.

Immediately after the FP, the collimated beam passes through a CaF_2 window and into a dual cryogen dewar (International Cryogenics Inc.), containing one liquid (T=77 K) and one solid (T=48–55 K) nitrogen vessel. The liquid nitrogen vessel decreases the heat load on the solid nitrogen canister, which attaches to the optical work surface. Inside the dewar, the beam passes through a cold (T~60 K) baffle tube that extends from the cold stop to the filter wheel. The filter wheel, which is rotated manually via a mechanical vacuum feedthrough, contains four $\frac{1}{2}$%–1% order-sorting filters (Barr Associates Inc.; Omega Optical Inc.). An antireflection coated Si doublet camera lens (Optics for Research Inc.) with a 24 mm focal length focuses the beam onto a 1 mm diameter InSb photovoltaic detector (Cincinnati Electronics Corp.).

The combination of a fast camera lens and a large detector face results in a large instrumental beamsize (see Table 1) denoted by Θ,

$$\Theta = 65'' \left(\frac{P_{\rm tel}}{4''.32 \ {\rm mm}} \right) \left(\frac{f_{\rm coll}}{457 \ {\rm mm}} \right), \quad (1)$$

where $P_{\rm tel}$ is the plate scale of the telescope and $f_{\rm coll}$ is the focal length of the collimator. Occasionally, to achieve

© 1995. Astronomical Society of the Pacific

© Astronomical Society of the Pacific • Provided by the NASA Astrophysics Data System

1995PASP..107..184L

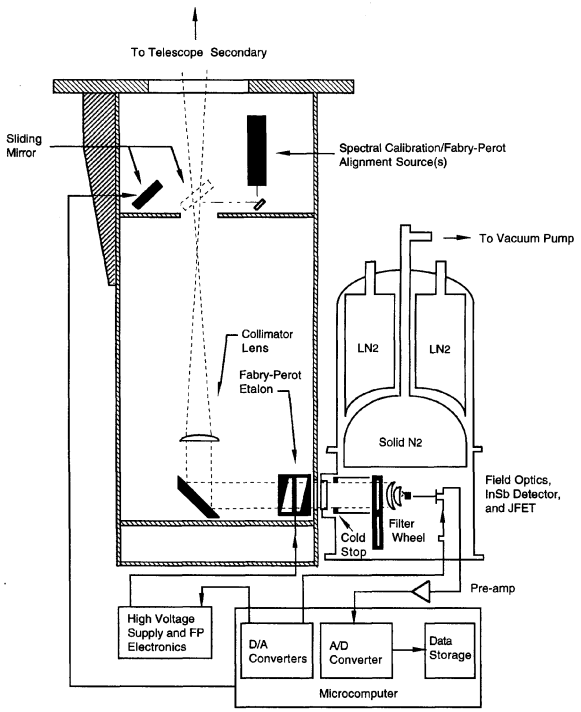

FIG. 1—Schematic representation of the Fabry-Perot spectrometer.

TABLE 1
Summary of Instrument Characteristics

Wavelength range	1.4 – 2.4 μm	
	Point source	Extended source[a]
Spectral resolution		
at 1.6 μm	4000	3200
at 2.12 μm	3000	2400
Beamsize[b]		
McDonald 0.9 m	200″	
KPNO 1.3 m	160″	
Steward 1.55 m	85″	
McDonald 2.7 m	65″	
Palomar 5 m	20″	
Detector		
Material	InSb	
Diameter	1 mm	
Capacitance	50–60 pF	
Operating temperature	48–55 K	
Surface brightness sensitivity[c]	$< 10^{-6}$ ergs s^{-1} cm^{-2} sr^{-1}	

[a] Source fills a 65″ diameter beam.
[b] Camera lens focal length = 24 mm. Camera lens with focal length = 32 mm produces beamsize diameters that are 25% smaller than listed above (see §2).
[c] Total on-source integration time = 20 s at H or K. Ambient T = 5 C.

slightly higher spatial resolution, we use a Si meniscus camera lens that has a 32 mm focal length and reduces the beamsize diameter by 25% compared to the faster doublet lens. As shown in Table 1, the angular resolution is ideal for mapping regions that are several arcminutes or more in extent and provides a good match to much far-infrared and single-dish mm and cm wave data. Notice that since the beam size is large, the instrument requires no optics for guiding while observing on most modern telescopes.

A low noise integrating amplifier (Infrared Laboratories Inc., Model JF-4) with a nondestructive read-out integrates the photogenerated charge on the detector capacitance. The JF-4 amplifier consists of a hybrid circuit containing a balanced junction field-effect transistor (JFET) with a voltage gain of 0.8–0.9. An external reset pulse removes the collected charge from the integrating gate before each exposure. A pre-amplifier (Infrared Laboratories Inc., Model RS-1) amplifies the voltage signal from the JFET with gain of 100, and a 16-bit A/D converter (Analogic Corp.) reads the final signal. The data are stored on the hard drive of a 486 PC and backed up on floppy disks.

3. ACHIEVEMENT OF OPTIMAL SURFACE BRIGHTNESS SENSITIVITY

3.1 Light Path

For observations of unresolved spectral lines with a background-limited system, the signal-to-noise ratio S/N depends on the throughput U, or étendue,

$$U = A_p \Omega_b \Gamma_{\rm tot}, \qquad (2)$$

where A_p is the collecting area of the primary mirror, Ω_b is the solid angle field of view of the system (assuming $\Omega_{\rm source} \gg \Omega_b$), and $\Gamma_{\rm tot}$ is the fractional transmission of the optical components in the telescope and the spectrometer. The spectral line S/N is proportional to

$$\left[\frac{U}{\Sigma_i \varepsilon_i (\Delta\lambda)_i B(T_i)}\right]^{1/2}$$

where, respectively, ε_i and $B(T_i)$ are the emissivity and blackbody source function for the ith surface in the beam and $(\Delta\lambda)_i$ is the effective noise bandwidth of the system between the detector and the surface in question. Therefore, we can enhance the system sensitivity to diffuse line emission if we maximize U, minimize the emissivity ε of the telescope and instrument, and reject as much background radiation and as little of the source signal as possible. With these factors in mind, we designed the light path and optical components to restrict and lower the amount of background radiation falling on the detector while, at the same time, providing high throughput and sufficient spectral resolution to measure line strength accurately.

As shown in Fig. 1, the light path is very simple with few warm optical elements to contribute to light loss and background radiation. Looking out along the optical path from the position of the detector, the optical configuration eliminates direct view of warm elements other than optical surfaces. One of the warm components is the refractive collimator, which images the exit pupil at a cold stop (the Lyot stop) just past the FP and inside the dewar. Consequently, the collimated beam is very near its minimum diameter at the FP and suffers no vignetting.

The very short focal length of the camera lens and the large detector face provide a very large $A\Omega$ at the detector but can produce large aberrations at the detector focus and

© Astronomical Society of the Pacific • Provided by the NASA Astrophysics Data System

1995PASP..107..184L

lead to significant light loss. Use of a collimating lens eliminates the coupling loss due to coma at the detector, unlike an off-axis paraboloidal mirror, for example. We find that, for a source that fills our beam, an off-axis paraboloid tilted by only a few degrees introduces a 40% loss in throughput due to coma. The light loss is most pronounced for the outer rays that lie farthest off-axis at the instrument focal plane. Since the collimating lens virtually removes coma over the entire focal plane, the camera lens becomes the dominant source of aberration, primarily spherical aberration. The doublet design of the camera lens minimizes the spherical aberration. Minimizing spherical aberration and coma sharpens the beam profile, lowers the background, and enhances the throughput.

The Fabry-Perot filter limits the noise bandwidth for the sky and all system components beyond the FP to $(\Delta\lambda)_i \simeq \frac{1}{2}\pi\Delta\lambda$ where $\Delta\lambda$ is the FWHM of the FP instrumental profile. Radiation emitted by the FP itself is restricted by the $\frac{1}{2}$%–1% 60 K order sorting filters. To ensure that most of the stray light that enters the dewar passes through the FP filter, we have placed the FP as close as possible to the dewar window (Geballe 1974). This placement reduces the effects of scattering and multiple reflections into the beam between the FP and the dewar window, because the FP is essentially a mirror off-band and images the cold surfaces inside the dewar. To keep the background radiation in the dewar to a minimum, we have taken care in baffling the mechanical feedthrough for the filter wheel and the light path in the dewar. We have blackened all cold reflective surfaces on the work surface with a carbon-based paint. At the end of the light baffle tube in the dewar, we have placed a knife-edge cold stop, with adjustable diameter for each telescope configuration.

The clear aperture diameter of the FP etalon is 32 mm, which matches the typical diameter of the collimated beam. In addition, the FP interferometer satisfies two additional system requirements: high throughput and high spectral resolution. The etalon plates are coated to transmit 70%–80% of the light at resonance. Specifically, the plate reflectivity r is 93% (within the FP cavity), which produces reasonable (~40) reflection finesse F_r,

$$F_r = \frac{\pi r^{1/2}}{1-r}, \tag{3}$$

and high (>70%) transmission $\Gamma_{\rm FP}$,

$$\Gamma_{\rm FP} = \left(\frac{1-r-a}{1-r}\right)^2, \tag{4}$$

where a is the percentage losses from absorption and scatter (typically ≤0.2%/surface). Higher values of r sacrifice transmission for improved reflection finesse, e.g., for r=97%, $F_r \sim 100$, $\Gamma_{\rm FP} \sim 40\%$.

For an FP, we can estimate the spectral resolving power $\lambda/\Delta\lambda$ from

$$\lambda/\Delta\lambda = mF_{\rm eff}, \tag{5}$$

where m is the order of interference and $F_{\rm eff}$ is the effective finesse of the FP. The value of $F_{\rm eff}$ is given by

$$F_{\rm eff}^{-2} \approx F_r^{-2} + F_{pp}^{-2} + F_{\rm ang}^{-2} \tag{6}$$

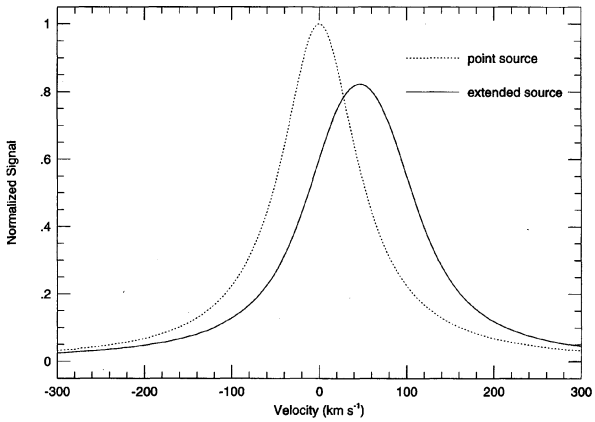

FIG. 2—Instrumental profile of an FP interferometer in velocity units for a point source (incident angle to the FP=0) at the instrument focal plane and, likewise, for an extended source (incident angle=0.025 rad) that fills our beam. The calculated profiles assume m=93, F_r=30, and $F_{\rm ang}$>90.

where F_{pp} is the parallelism (alignment) and planeness finesse and $F_{\rm ang}$ is the finesse arising from the range of angles of the incident beam at the FP plates. In Eq. (6), the value of F_r is a constant. The contribution of F_{pp} (>90) to $F_{\rm eff}$ is small if we frequently realign the FP plates (see Appendix).

The third element in the effective finesse, $F_{\rm ang}$, forms part of a complex tradeoff in the instrument design. The high spectral resolution of our FP restricts the thermal background that the detector sees. Also, in many cases, high resolving power helps to avoid contamination of spectral lines by telluric OH lines (see Sec. 3.3). Conservation of energy, however, requires that $A\Omega$ be a constant through the system. The size of the primary and the telescope beam, for a given collimated beam diameter, therefore determine the angular divergence of the collimated beam as it passes through the Fabry-Perot. The rays from an extended source that fills the beam cover a range of incident angles, and with each angle, the FP passes a slightly different wavelength. As a result, the instrumental profile for an extended source is broader than the point-source profile (the integrated profile is unchanged). The calculated instrumental profiles in Fig. 2 illustrate this effect. From the calculated profiles, $F_{\rm eff}$=23 for an extended source, which compares to $F_{\rm eff}$=29 for a point source. (Notice that, with respect to the point-source profile, the wavelength of maximum transmission for the extended source shifts by +45 km s^{-1}, since for a given plate spacing, a nonzero incident angle decreases the transmitted wavelength and thus shifts the wavelength scale to longer wavelengths.) In Table 1, we list the measured resolving power for both a point source and an extended source.

We have chosen our Ω_b to be as large as possible consistent with $F_{\rm ang}$ not dominating $F_{\rm eff}$. A larger étendue would be possible either by lowering $F_{\rm eff}$ and thereby increasing the background and OH line confusion or by increasing the size of the collimated beam. A larger FP, however, would have been too expensive for the current instrument's budget. The étendue achieved by this instrument is more than 10 times what could be reasonably achieved with a long-slit grating spectrometer of comparable spectral resolution.

© Astronomical Society of the Pacific • Provided by the NASA Astrophysics Data System

1995PASP..107..184L

3.2 Detector and Read-Out Electronics

To realize the gain in surface brightness sensitivity stemming from high throughput, the system sensitivity must approach the background limit within a reasonable integration period, which requires a low read noise detector and amplifier. To this end, we use an integrating detector/amplifier circuit, which contributes noise only when read-out. Our need for sensitivity to extended source line emission also calls for an integrating circuit, since the signal is DC coupled to the detector. (Standard AC coupled detection reduces sensitivity in cases where the chopper throw is less than the scale length of the extended line emission.) Integrating circuits also offer excellent DC stability for raster mapping large-scale sources without frequent sky measurements.

We explicitly chose the detector/amplifier elements of our integrating system for their low read noise characteristics. Both detector and amplifier have low input capacitance. Our InSb photovoltaic detector is one of the COBE series detectors (Wimmers and Smith 1984). A normal 1 mm diameter InSb detector (optimized for RA product, where R and A are the impedance and active surface area of the detector, respectively) has a capacitance of 150–200 pF. The zero-bias diode capacitance of a COBE series detector, however, is 50–60 pF. The input capacitance of the JFET integrating amplifier, which adds in parallel to the detector capacitance, is only 7.5 pF. The combined capacitance of the detector and amplifier is very low given the large active area of the detector.

The detector and JFET amplifier also have very high input impedance R. When cooled to solid nitrogen temperatures ($T\sim55$ K), the detector impedance is $>10^{12}$ ohm. For comparison, R is only $\sim10^{8}$ ohm at 77 K. Cooling the detector to 55 K is generally sufficient to minimize the influence of the dark current on surface brightness sensitivity. The high impedance of the integrating amplifier, which is made only of capacitors and FETs, prevents charge leaking away through the amplifier and buffers the signal from external noise sources during integration. The buffer also allows the voltage to be read nondestructively, which enables the use of digital noise-reduction techniques.

During an integration, the charge generated by the photocurrent and dark current collects on the combined capacitance of the detector and the gate of the JFET; the preamplifier amplifies the voltage signal (accumulated charge divided by the capacitance) from the JFET; and an A/D converter samples the final signal at a rate of 10 kHz. The slope of the sample voltage as a function of time corresponds to the detected signal. Following Chapman et al. (1990), we have coded a real-time routine that takes multiple samples of the voltage and finds the slope of the best-fitting straight line through the points using a least-squares fit. If we assume that read noise dominates over the other noise sources, the statistical read noise $\sigma_{\rm read}$ is calculated from

$$\sigma_{\rm read}=\sigma_{\rm sample}\left(\frac{12}{Bt}\right)^{1/2}\ \text{electrons}, \tag{7}$$

where $\sigma_{\rm sample}$ is the rms error of each sample and B is the sample rate (10 kHz). Thus, using this noise reduction algorithm, the read noise actually *decreases* with time.

Before the start of an exposure, we send a pulse to a reset circuit, which ties the detector circuit to ground and removes the collected charge from the integrating gate of the JF-4. However, when looking at a very bright lamp, for example, some charge can still remain after the reset, which adds to the collected charge for the integration that follows and biases the slope of the voltage signal. The resultant data point appears as a "spike" in the spectrum. We find that the first sample voltage for these "spikes" are offset from the values for the unbiased data. We have coded a real-time filter whereby we use the first sample voltage to flag the "spikes," which are discarded and never stored. We immediately reset the detector and start a new integration. By removing this source of noise, we greatly enhance the spectral S/N.

3.3 Measured Sensitivity

Depending on the integration time and wavelength region, the instrument sensitivity is limited by read noise [Eq. (5)] or shot (Poisson) noise due to variations in the random rate of generation of charge carriers, namely background shot noise and dark-current shot noise (see, for example, Vincent 1990; Kitchin 1991). The background shot noise $\sigma_{\rm back}$ refers to the carriers generated by arriving background photons and is given by

$$\sigma_{\rm back}=(2\,\eta\phi_b t)^{1/2}\ \text{electrons}, \tag{8}$$

where η is the detector quantum efficiency (60%–70% for InSb) and ϕ_b is the incident photon rate in s^{-1}. In the absence of photon illumination, charge carriers are thermally generated, producing dark-current shot noise $\sigma_{\rm dark}$,

$$\sigma_{\rm dark}=\left(\frac{2I_{\rm dark}t}{q}\right)^{1/2}\ \text{electrons}, \tag{9}$$

where q is the electronic charge and $I_{\rm dark}$ refers to the dark current. The dark current depends on the temperature T and impedance R of the detector according to

$$I_{\rm dark}\propto\frac{T}{R},\quad R\propto\exp\left(-\frac{C}{T}\right),$$

where C is a constant relating to the energy band gap of InSb. The total noise $\sigma_{\rm total}$ is

$$\sigma_{\rm total}=(\sigma_{\rm back}^2+\sigma_{\rm dark}^2+\sigma_{\rm read}^2)^{1/2}. \tag{10}$$

From Eqs. (7)–(9), we see that the read noise ($\propto t^{-1/2}$) dominates the total noise for short integration times, while for long integration times, the background and dark-current shot noise ($\propto t^{1/2}$) becomes increasingly important.

In Table 2, we list typical values for the read noise, dark current, and background flux at 1.6 and 2.12 μm, along with the total noise as given by Eqs. (7)–(10). As shown in Table 2, the read noise is 200 e for a 2 s integration, or the equivalent of a per pixel read noise of 6 e for a 1 mm diameter array with 30 μm pixels. Likewise, our measured dark current of 1.1×10^{4} e/s corresponds to a per pixel value of 12 e/s for a 1 mm diameter, 30 μm pixel array. For a single exposure at 1.6 μm, we find that $\sigma_{\rm read}$ dominates the system noise for $t<2$ s, and $\sigma_{\rm dark}$ dominates for $t>2$ s. At 2.12 μm, the

© Astronomical Society of the Pacific • Provided by the NASA Astrophysics Data System

1995PASP..107..184L

TABLE 2
Typical Noise Parameters

	Current system	Future system[f]
Read noise[a]	200 e	200 e
Dark current	1.1×10^4 e/s[e]	1 e/s[g]
Background flux[b]		
at 1.6 μm	$< 10^3$ γ/s	$< 10^3$ γ/s
at 2.12 μm	8.5×10^5 γ/s	$(2\text{–}4) \times 10^5$ γ/s
Total noise		
at 1.6 μm[c]	290 e	200 e
at 2.12 μm[d]	1100 e	600–800 e

[a] Integration time $t = 2$ s (read noise $\propto t^{-1/2}$; see §3.2).
[b] Ambient $T = 5$ C, $\eta = 0.6$. Instrument attached to McDonald Obs. 2.7-m telescope.
[c] $t = 2$ s.
[d] $t = 1$ s.
[e] Detector $T = 50$ K.
[f] Cool FP to −78 C; cool detector to ≤ 35 K.
[g] Estimated from $I_{dark}(T)$ (see §3.3) after normalizing to $(RA)_{det} = 10^8$ ohm cm^2 for $T = 65$ K. Actual value will be higher.

system is read-noise limited for $t<1$ s and background shot noise limited thereafter.

Thermal emission from the ambient temperature FP within the bandpass of the order-sorting filter accounts for 50%–75% of the total background radiation. If we cooled the FP to <-50 °C, using dry ice (−78 °C), for example, we could eliminate the thermal contribution from the FP for all reasonable ambient temperatures at the cost of making the FP inaccessible and adding one extra window to the optical train. In addition, cooling the detector to below 35 K would reduce the dark current (see Table 2) and enhance the H-band sensitivity for $t>2$ s. For comparison, Table 2 gives the expected total noise upon making these future improvements to the system.

The noise of real interest, however, is the noise left after sky-subtracted spectra of the line and continuum have been coadded. In this case, a major source of noise arises from variations in the atmospheric background. One such source is the nonthermal OH airglow line emission, which limits the sensitivity in the J and H windows and in the short wavelength half of the K window. In Figs. 3 and 4, we show the OH lines in the vicinity of the [Fe II] 1.644 μm line and the H_2 $v=1-0$ $S(1)$ line at 2.121 μm measured with our spectrometer. Ramsay et al. (1992) have shown that the OH lines vary significantly on time scales of 5 to 15 min, although the amplitude change is not constant for each line. To avoid misubtraction of the OH lines, the time Δs between sky reference measurements should be much shorter than this time scale. In the low background, read-noise limited regime, infrared arrays require long on-chip exposure times of up to

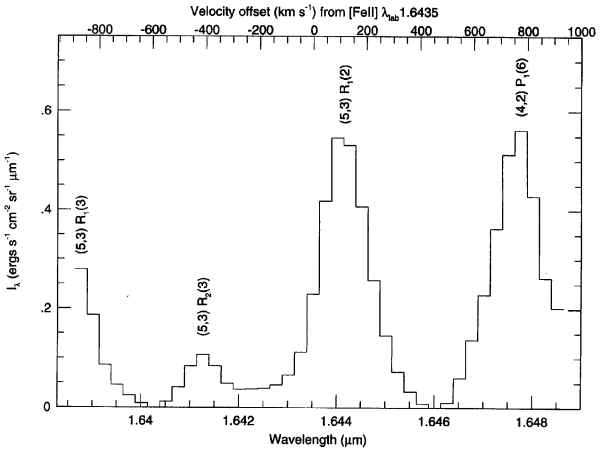

FIG. 3—Section of the night sky spectrum in the proximity of the [Fe II] 1.6435 μm line. We label the transitions of identified OH airglow lines.

tens of minutes to achieve a major gain in S/N ($\propto t^{1/2}$ in the shot-noise limit). In less than a few seconds, read noise no longer limits the sensitivity of our single-detector system. We can therefore switch rapidly between source and sky (small Δs), which is a definite advantage in beating the effects of OH airglow. In many cases, the resolving power of the FP also helps to avoid spectral contamination by OH lines. Spectral lines that do fall on an OH feature, e.g., the [Fe II] 1.644 μm line (see Fig. 3), require very rapid switching.

Rapid switching also suppresses the $1/f$ noise from fluctuations in the thermal sky background, owing to fluctuations in the atmospheric transmission and, hence, emissivity. As with the OH airglow, the degree to which $1/f$ noise limits the sensitivity is partly a function of Δs. Figure 5 shows a plot of 1σ surface brightness sensitivity with integration time. The sky measurements were acquired by nodding the telescope without chopping the secondary. In Fig. 5, we see that from 0 to 20 s, the 1σ surface brightness level decreases with integration time, dropping as $t^{1/2}$ as expected in the back-

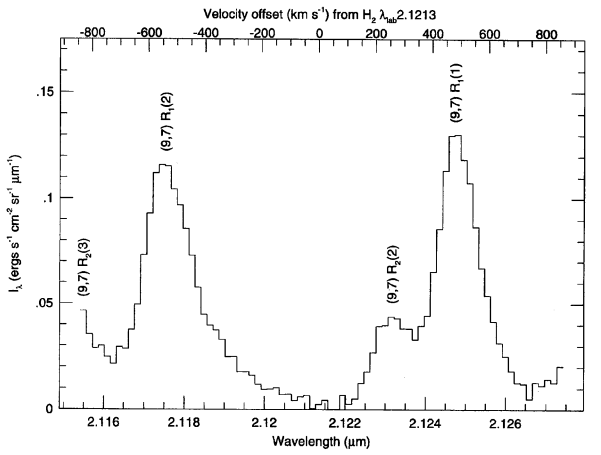

FIG. 4—Section of the night-sky spectrum in the proximity of the H_2 $v=1-0$ $S(1)$ line at 2.1213 μm. We label the transitions of identified OH airglow lines. The intensity calibration of the OH lines relative to the lines in Fig. 3 is highly uncertain (see Sec. 3.3).

© Astronomical Society of the Pacific • Provided by the NASA Astrophysics Data System

1995PASP..107..184L

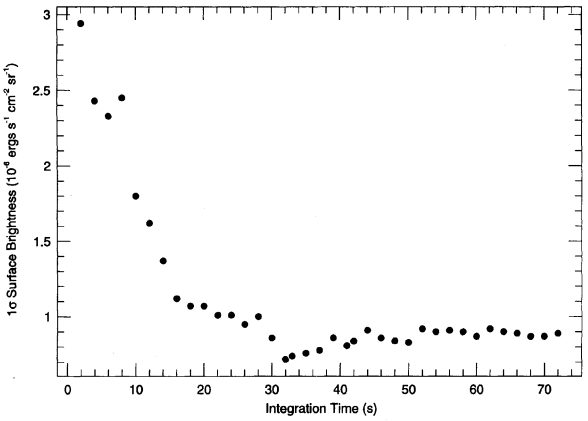

FIG. 5—Plot of the change in 1σ surface brightness sensitivity as a function of integration time, obtained by coadding 2.12 μm spectra of the galaxy M51.

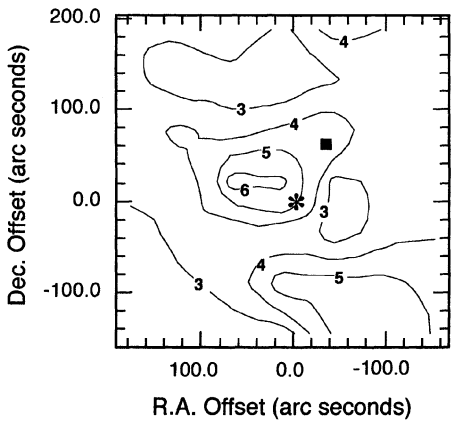

FIG. 7—H_2 $v=6-4$ $Q(1)$ map of the Orion H II region/molecular cloud interface. The peak contour level corresponds to a surface brightness of 6.4×10^{-6} ergs s^{-1} cm^{-2} sr^{-1} in a 65″ beam. The 0,0 position is at θ^1 Ori C. We have marked θ^1 Ori C and the BN-KL outflow by an asterisk and a square, respectively.

ground limit. However, after 30 s, $1/f$ noise places a fundamental limit on the minimum attainable sensitivity ($\sim10^{-6}$ ergs s^{-1} cm^{-2} sr^{-1}). We can lower the imposed sensitivity floor further by decreasing Δs, for example, by using a chopping secondary with sufficient throw. We estimate that our $1/f$ noise-detection limit falls at least an order of magnitude below that of typical array-grating spectrometers and imaging systems due to the inherent difference in Δs.

4. OBSERVATIONAL PROCEDURES

As explained in the Appendix, we can control the plate spacing of the FP etalon by applying a voltage to three piezoelectric translators. Prior to the observations, we determine the relation between the applied voltage and the plate spacing. For the wavelength calibration, we use emission

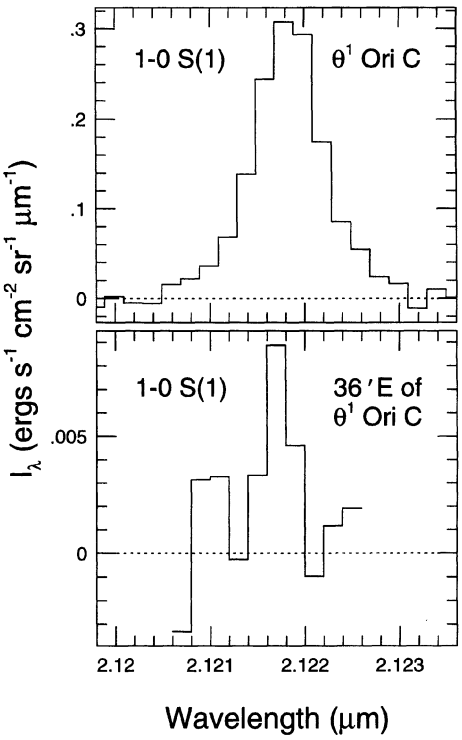

FIG. 6—(top) 2.121 μm $v=1-0$ $S(1)$ line toward θ^1 Ori C ($\alpha_{1950}=5^h32^m49\overset{s}{.}0$, $\delta=-05°25'15''$). The line strength is $(3.03\pm0.10)\times10^{-4}$ ergs s^{-1} cm^{-2} sr^{-1} in a 49″ beam. The line is unresolved ($\lambda/\Delta\lambda\sim2400$), and we have subtracted the stellar continuum from the spectrum. (bottom) 2.121 μ $mv=1-0$ $S(1)$ line 36′ east of θ^1 Ori C. The line strength is $(3.0\pm0.8)\times10^{-6}$ ergs s^{-1} cm^{-2} sr^{-1}.

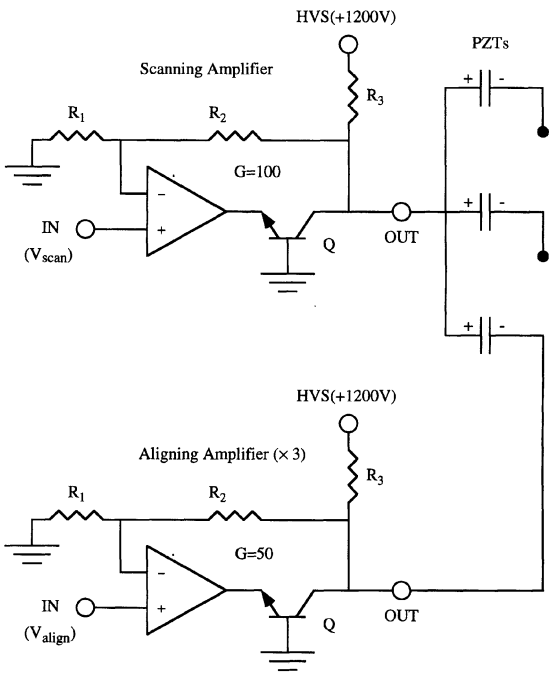

FIG. 8—Simplified noninverting feedback op-amplifier circuit diagram for the scanning amplifier and one of the aligning amplifiers. The gain (G) is determined by $G=1+R_2/R_1$. One regulated high voltage supply (HVS) supports the four circuits, and each R_3 divides the output power.

© Astronomical Society of the Pacific • Provided by the NASA Astrophysics Data System

1995PASP..107..184L

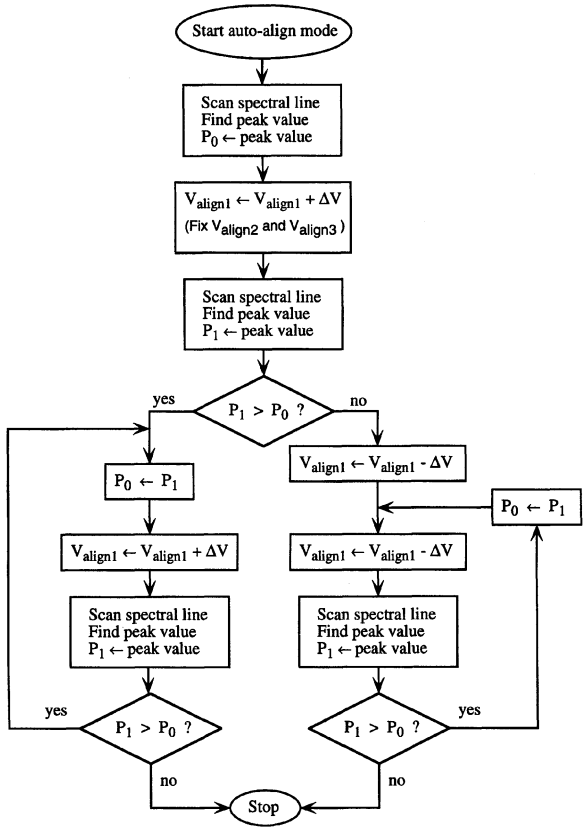

FIG. 9—The algorithm of the automatic alignment program. We use a trail and error approach to find the best V_{align1}. The program monitors the alignment status by checking the peak signal value (P_i) of the observed reference spectral profile. Running this routine in turn for V_{align2} and V_{align3}, we can maintain optimum alignment of the FP etalon.

lines of helium, neon, argon, or krypton depending on the wavelength region. Standard spectral calibration lamps (Oriel Corp.) or the discharge from a He–Ne laser serve as emission-line sources.

Before we acquire an astronomical spectrum, the FP plates are aligned automatically using the algorithm outlined in the Appendix. We call the auto-alignment routine as often as necessary to maintain parallelism, which is typically every 10 to 20 minutes under normal observing conditions. With the FP aligned and the sliding mirror inserted into the optical axis of the telescope (see Fig. 1), we scan across the desired spectral range. Often, a spectral calibration line lies very near the astronomical line of interest. By scanning the spectral lamp before and after a sequence of observations, we note changes in the wavelength position of the reference line and can therefore correct for occasional drifts in the wavelength scale in the data reduction.

In our standard observing mode, we obtain a preset number of scans across the line profile while looking at the source, then nod the telescope to a predetermined sky position, and repeat the same sequence (beam switching). For extended (>a few arcminutes) sources, we generally beam switch without chopping to remove the background signal, since the maximum chopper throw of most telescopes is only a few arcminutes. A typical background-limited spectrum in the K band requires ~10 s of integration time. Thus, when beam switching, we can acquire the off-source spectra very close in time to the on-source spectra and reduce the effects of atmospheric fluctuations.

For sources with angular size less than a few arcminutes, we can obtain the on- and off-source spectra virtually simultaneously using a chopping secondary (if one is available). The ability to monitor the FP alignment and to correct for wavelength drift allows us to fix the FP at the peak wavelength of the line and chop the secondary back and forth between the source and sky positions. When mapping, we can use this "reconnaissance" mode to locate quickly the strongest emission regions. Later, we can then obtain spectral-line profiles for these positions. Frequency switching is a related technique whereby we switch the FP back and forth between the wavelength of the line peak and a nearby, uncontaminated portion of the continuum. Like beam switching, this method is suited for large-scale mapping but does so much more rapidly. Like the "reconnaissance" mode, frequency switching requires frequent checks of the FP alignment, since we measure the line peak intensity only. For the same reason, frequency switching is not appropriate for measuring weak emission lines that fall near an OH feature.

A single software program executes the various observing modes, controlling the instrument and collecting data with D/A and A/D converters, respectively. The control program also crudely coadds and displays the background-subtracted data, allowing us to react to any real-time problems, changing conditions, or observational results. The final data set consists of on- and off-source scans, wavelength-calibration source scans, and standard star measurements for flux calibration, as well as information about the type of scan, time of observation, wavelength setting, etc. We have developed data reduction software which edits spikes, arithmetically manipulates spectra, performs error analysis and wavelength and flux calibration, and calculates baseline fits and integrated line strengths. In the data reduction, we can also perform corrections to the wavelength and flux calibration arising from the difference in spectral line profiles for a point and an extended source (Fig. 2) and due to known flux leakage from adjacent FP orders.

5. SAMPLE DATA

Currently, we have narrowband order-sorting filters for Brγ 2.166 μm, [Fe II] 1.644 μm, and six H_2 lines: 1.601 μm $v=6-4$ $Q(1)$, 1.613 μm=$v=5-3$ $O(3)$, 1.616 μm $v=6-4$ $Q(3)$, 2.121 μm $v=1-0$ $S(1)$, 2.247 μm $v=2-1$ $S(1)$, and 2.423 μm $v=1-0$ $Q(3)$. We have observed the large-scale emission of one or more of these lines in a variety of sources, such as the Orion A molecular cloud (Luhman et al. 1994), the ρ Oph dark cloud, the Galactic Center, the supernova remnant IC 443, and the starburst galaxy M82. To date, we have used our FP spectrometer with the McDonald Obs. 0.9-m and 2.7-m, the KPNO 1.3-m, and the Steward Obs. 1.55-m telescopes.

In Figs. 6 and 7, we present sample data that demonstrate our ability to detect and map faint (~10^{-6}

© Astronomical Society of the Pacific • Provided by the NASA Astrophysics Data System

1995PASP..107..184L

ergs s^{-1} cm^{-2} sr^{-1}) H_2 line emission in the near infrared. Figure 6 displays spectra of the unresolved H_2 $v=1-0$ $S(1)$ line toward θ^1 Ori C in Orion and toward the outer part of the Orion A cloud. We acquired the data using the McDonald 2.7 m in 1994 February. Figure 7 shows a map of the diffuse H_2 $v=6-4$ $Q(1)$ emission in the inner $6'\times6'$ of Orion A (Luhman et al. 1994), which we obtained in 1994 February using the Steward Obs. 1.55 m.

The $v=1-0$ $S(1)$ line strength ($[3.03\pm0.10]\times10^{-4}$ ergs s^{-1} cm^{-2} sr^{-1}) toward θ^1 Ori C agrees with previous observations smoothed to our spatial resolution (Garden 1986). The $v=1-0$ $S(1)$ emission toward the outer Orion cloud required a total (source+sky) exposure time of 20 s per channel for a $\geq3\sigma$ detection. Thus, with only a few minutes total integration, we can detect very extended line emission as weak as a few times 10^{-6} ergs s^{-1} cm^{-2} sr^{-1}. Finally, notice in Fig. 7 the uniformity of the $v=6-4$ $Q(1)$ emission, which only varies by a factor of 2 over $6'\times6'$, indicating that observations using small chopper throws ($1'-2'$) would have suppressed the $v=6-4$ $Q(1)$ line. Two-dimensional array imaging or spectroscopy relying on sky subtraction images or spectra well separated in time would not have been sensitive to much of the $v=6-4$ $Q(1)$ emission.

6. SUMMARY

We have developed a high-throughput, low-noise Fabry-Perot spectrometer for operation at near-infrared wavelengths. The instrument is optimized for the detection of diffuse line emission in very extended ($>1'$) sources. In particular, the Fabry-Perot spectrometer combines the following features: (1) minimized light loss from the telescope to the detector; (2) optics that eliminate aberrations at the detector focus; (3) moderate resolving power ($\lambda/\Delta\lambda\sim2500$) to restrict thermal background radiation; (4) a very short focal length camera lens coupled with a large detector face for large $A\Omega$; (5) a detector and integrating amplifier with low input capacitance/impedance; (6) a sampling scheme that reduces read noise as exposure time increases; (7) an observing routine that efficiently and reliably removes sky background, even for every extended objects; and (8) the rapid ability to monitor and maintain FP etalon alignment.

In the K band, the system is background shot-noise limited for $t\geq1$ s, which allows us to obtain sky reference spectra very close in time to the source spectra without sacrificing S/N. This is a key advantage over array systems in overcoming the limitations placed on surface-brightness sensitivity due to fluctuations in the night-sky emission. Likewise, in the H window where night-sky variations often dominate the total noise, the ability to monitor rapidly the sky emission is crucial for detecting very diffuse line emission. We have used our FP spectrometer successfully on multiple telescopes and have acquired data that verify the instrument sensitivity to low-level line emission. In the future, we expect to increase the sensitivity still further by lowering the operating temperature of the detector and the FP.

We wish to thank J. H. Lacy and T. R. Geballe for very helpful comments during several phases of this work. We also thank G. Barczak, J. F. Harvey, and J. Welborn for their assistance in the construction of the spectrometer and design of the FP control electronics. This work was supported by the David and Lucile Packard Foundation through a fellowship to D.T.J. and by a NASA Graduate Traineeship Grant No. NGT-50998 held by M.L.L.

APPENDIX: THE FABRY-PEROT INTERFEROMETER

The spectrometer system uses a Burleigh Inc., TL-38 Tunable Etalon. In this FP, two reflecting etalon plates are separated by ~100 μm, and the reflectance of each plate surface is about 93%. The etalon plates are permanently mounted in two holders. The rear mirror holder is mechanically tilted by adjusting two spring-loaded mounting screws. The front mirror holder is attached to a tunable drive ring that is supported by three piezoelectric transducers (PZTs). Applying a DC voltage to the three PZTs independently aligns the front plate with respect to the rear plate, and driving all three PZTs simultaneously changes the plate spacing parallel to the optical axis. To manipulate the etalon plates, three alignment voltages (0–500 V) are applied to the negative poles of the PZTs individually, and one scan voltage (0–1000 V) is applied to the positive poles simultaneously (Fig. 8). We can integrate the signal at a fixed scanning voltage and construct a spectral profile by increasing or decreasing the scanning voltage step by step.

To manipulate the PZTs, we built a high-voltage DC amplifier, which is used between the PZTs and the D/A interface board (Strawberry Tree Inc., Model DAA-10120) in the computer. The D/A board has four 0 to 10 volt output channels: three for the aligning channels (50 gain) and one for the scanning channel (100 gain) of the HV amplifier. The HV amplifier box has a regulated high-voltage supply (Bertan Associates Inc., Model 602C-15P) and four independent noninverting feedback amplifier circuits, each of which contains an identical op-amp (Newark Electronics, Model TL082CP) as depicted in Fig. 8. A power transistor between the op-amp and the output channel provides the high voltage output.

Part of the instrument control software is an automatic alignment routine. The program monitors the FP alignment by checking the spectral profile of a reference source, either a He, Ne, Ar, or Kr spectral line. As the two plates become parallel, the FWHM of the observed profile decreases, and the peak signal P_i increases. We use the peak signal to monitor the alignment.

Figure 9 shows a flow chart of the automatic alignment program. First, the program scans the reference spectral line. From the scanned data, a peak signal value of the line is stored in a buffer. Next, one of the three aligning PZT voltages ($V_{\rm align1}$) is adjusted while fixing the other two voltages ($V_{\rm align2}$ and $V_{\rm align3}$), and the reference line is scanned again. If the new peak value is larger than the previous one, the program adjusts the aligning voltage and scans again. This procedure is repeated until the peak signal is maximized. In the same manner, the other two aligning voltages are adjusted in turn. It takes less than 30 s to align the FP with this program,

© Astronomical Society of the Pacific • Provided by the NASA Astrophysics Data System

1995PASP..107..184L

which we typically call every 10 to 20 min during observations. Sudden changes in the ambient temperature due to intermittent winds, for example, affect the length of the piezoelectric crystals, which can misalign the FP plates and induce wavelength drift on a time scale of less than a few minutes. A three-sided house shelters the etalon from direct wind to reduce the drift rate.

REFERENCES

Chapman, R., Beard, S. M., Mountain, C. M., Pettie, D. G., and Pickup, D. A. 1990, in Instrumentation in Astronomy VII, ed. D. L. Crawford (Washington, SPIE), p. 34

Garden, R. 1986, Ph.D. thesis, University of Edinburgh

Geballe, T. R. 1974, Ph.D. thesis, University of California, Berkeley

Hoffman, A. W., and Woolaway, J. T. 1994, in Infrared Astronomy with Arrays: The Next Generation, ed. I. S. McLean (Kluwer, Dordrecht), p. 369

Kitchin, C. R. 1991, Astrophysical Techniques, (New York, Adam Hilger)

Luhman, M. L., Jaffe, D. T., Keller, L. D., and Pak, Soojong 1994, ApJ, 436, L185

Maihara, T., Iwamuro, F., Yamashita, T., Hall, D. N. B., Cowie, L. L., Tokunaga, A. T., and Pickles, A. 1993, in Infrared Detectors and Instrumentation, SPIE Conference Series No. 1946

Ramsay, S. K., Mountain, C. M., and Geballe, T. R. 1992, MNRAS, 259, 751

Vincent, J. 1990, Fundamentals of Infrared Detector Operation and Testing (New York, Wiley-International)

Wimmers, J. T., and Smith, D. S. 1984, in SPIE Infrared Technology X, 510, 21

© Astronomical Society of the Pacific • Provided by the NASA Astrophysics Data System